Nano Research

Open Access

Research Article

Nanofiber-reinforced $CoFe_2O_4$/graphene composite aerogel as broadband electromagnetic wave absorber

Shuang Xu[1,2], Qinghai Liu[2], Zhaoliang Yu[2], Lijun Li[2], Xiaodong Dai[2] ✉, Shuyan Yu[1], and Congju Li[1,3] ✉

[1] *School of Energy and Environmental Engineering, University of Science and Technology Beijing, Beijing 100083, China*
[2] *State Key Laboratory of NBC Protection for Civilian, Beijing 102205, China*
[3] *College of Textiles, Donghua University, Shanghai 201620, China*

Cite this article: *Nano Research*, **2025**, *18*, 94907142. https://doi.org/10.26599/NR.2025.94907142

ABSTRACT: Graphene aerogel (GA) is a promising lightweight and high-performance material for electromagnetic wave absorption due to its ultra-light mass. However, the impedance matching and attenuation capabilities of GA are limited by its high conductivity and constrained attenuation paths. To address this limitation, magnetic materials are often combined with GA to enhance both impedance matching and attenuation performance. Nevertheless, little attention has been given to the influence of magnetic materials with varying morphologies on the electromagnetic wave absorption (EMA) properties. In this study, $CoFe_2O_4$ nanofibers were prepared via electrospinning technology as an alternative to commercial $CoFe_2O_4$ nanoparticles. Subsequently, $CoFe_2O_4$@GA composites were synthesized through a hydrothermal reaction in a graphene oxide (GO) solution. Moreover, the inclusion of ethylene glycol in the GO solution helped regulate the volume shrinkage of GA after the adding of $CoFe_2O_4$, thus preventing structural instability and fragmentation. The introduction of a small quantity of magnetic nanofibers significantly enhanced the EMA performance of the $CoFe_2O_4$@GA composite, increasing the strongest absorption from –34.5 to –53.5 dB and widening the maximum effective absorption bandwidth (EAB) from 8.0 to 8.7 GHz. Finally, the study revealed that $CoFe_2O_4$ nanofibers outperformed nanoparticles in electromagnetic wave loss mechanisms, including magnetic coupling, magnetic resonance, eddy current loss, and interface polarization. This finding provides valuable insights for the selection and optimization of magnetic component morphologies in EMA materials.

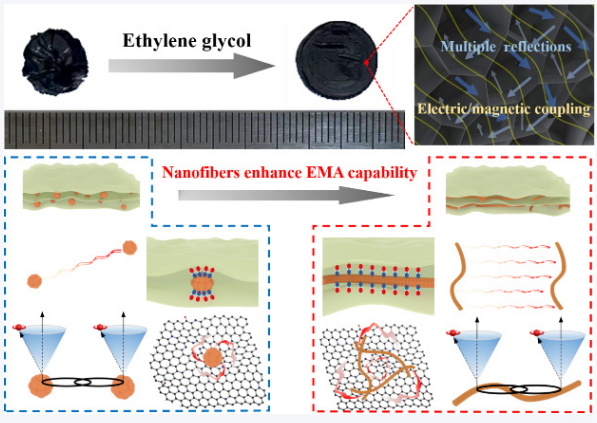

KEYWORDS: graphene aerogel, nanofiber, self-assembled, composite materials, magnetic coupling, electromagnetic absorption

1 Introduction

Since the initial discovery of graphene, its distinctive two-dimensional (2D) structure, extensive surface area, exceptional electrical conductivity, and tunable surface properties have facilitated rapid advancements in various fields. This progress has culminated in a diverse array of applications across multiple domains of materials science, including catalysts [1], supercapacitors [2], lithium-ion batteries [3], and fuel cells [4]. Furthermore, electromagnetic wave absorption (EMA) materials have garnered increasing attention due to the escalating issue of electromagnetic pollution and their considerable potential for both military and civilian applications [5]. Electromagnetic radiation can cause harm to the human body, and long-term exposure to the electromagnetic environment can increase the risk of cancer and cardiovascular disease [6]. In addition, electromagnetic radiation interferes with daily life, posing threats to information security and military defense [6, 7]. Therefore, there is a pressing need to develop lightweight and efficient universal EMA materials to mitigate the effects of pollution and interference from electromagnetic waves across a broad frequency range. In recent years, owing to graphene's unique interaction mechanisms with electromagnetic waves, both graphene and its composite materials have been extensively studied and engineered as novel EMA

Received: October 9, 2024; **Revised:** November 14, 2024
Accepted: November 18, 2024

✉Address correspondence to Congju Li, congjuli@126.com; Xiaodong Dai, dxd010@163.com

materials [8, 9]. However, prior research indicates that graphene's high electrical conductivity and robust conjugation result in suboptimal impedance matching and limited attenuation pathways [10, 11], significantly hindering its advancement as a high-performance EMA material. Consequently, it is imperative to implement strategies to improve the EMA performance of graphene.

It is widely recognized that the polarization of dipole moments plays a crucial role in enhancing the performance of EMA materials [12, 13]. The strategy of doping heteroatoms can significantly enhance the dipole polarization centers in graphene and is therefore commonly used to modify graphene for improved EMA performance [14–16]. Due to differences in electronegativity, doped heteroatoms influence the electrons in graphene's conjugated system, forming dipole polarization centers. By occupying the lattice positions of carbon atoms, heteroatoms create local stress in the surrounding area, leading to lattice distortion and the formation of additional chemical defects. These defect structures within graphene serve as dipole polarization centers, increasing the material's capacity for dipole polarization loss. Considering the synergistic electromagnetic loss effects of dielectric/magnetic hybrid materials, introducing magnetic materials into graphene broadens absorption mechanisms and optimizes impedance matching. This approach is also commonly employed to enhance graphene's EMA performance. Consequently, a variety of magnetic materials are not only introduced into graphene to create composites but are also meticulously engineered in diverse morphologies. For example, Wang et al. enhanced the EMA performance of reduced graphene oxide (rGO) aerogel by optimizing the ratio of $CoFe_2O_4$ nanoparticles to graphene [17]. Su et al. improved EMA performance and structural stability by incorporating Fe_3C particles with a yolk–shell structure into graphene [15]. Li et al. prepared a composite aerogel by combining magnetic FeN nanofibers with nitrogen-doped reduced graphene oxide, achieving outstanding EMA performance [18]. In addition to providing magnetic loss, magnetic components also establish a rich heterogeneous interface with graphene, inducing interface polarization and enhancing dielectric loss capacity. Beyond strategies aimed at enhancing dielectric and magnetic losses through modified graphene, the assembly and design of three-dimensional (3D) graphene aerogels (GAs) are widely utilized to enhance EMA performance. Graphene aerogels utilize graphene sheets as their fundamental building blocks, forming a three-dimensional network through cross-linking interactions [19]. This configuration produces interconnected porous structures with high surface areas, substantial pore volumes, and remarkable thermal and electrical conductivity [20, 21]. The porous structure of GA leads to multiple reflections and scatterings of electromagnetic waves, which enhances EMA performance. Additionally, GAs effectively prevent the stacking and agglomeration of graphene sheets, thereby maximizing material utilization. This characteristic endows GAs with significant potential in the research and development of lightweight and highly absorbent EMA materials. However, achieving outstanding performance in lightweight EMA materials with strong absorption across a wide frequency range through innovative design continues to pose a major challenge in academic research.

GAs have the characteristics of light weight, in contrast, magnetic materials generally have a larger density. This imposes significant limitations on the incorporation of magnetic components into GAs. Excessive incorporation of magnetic materials increases the density of GAs, undermining its advantages as an ultra-light material. Conversely, when the quantity of magnetic materials is minimal, it is challenging to utilize their loss capacity fully, resulting in limited improvements in EMA performance upon their incorporation. Furthermore, the self-assembly process of GAs is governed by the balance between van der Waals forces and charge interactions, further restricting the incorporation of magnetic components [22]. The excessive incorporation of magnetic materials may compromise the stability of the precursor solution, ultimately leading to the instability of GAs. In summary, the introduction of magnetic components into GAs necessitates that these components effectively utilize their magnetic loss capacity, even at minimal concentrations. Previous studies have explored various forms of magnetic materials [7, 23, 24]. However, the relative advantages of different forms of magnetic materials within the EMA mechanism remain poorly defined, leading to confusion in the structural design and applicability of these components in GAs. Consequently, it is more meaningful to compare the advantages of different magnetic components in GAs regarding their influence on the absorption mechanism, as this can inform the future structural design of magnetic components.

In this study, we present the assembly of graphene oxide with various morphologies of $CoFe_2O_4$ magnetic materials using a hydrothermal method. Subsequently, nitrogen atoms were doped into the graphene via nucleophilic substitution reactions, followed by liquid nitrogen freeze-drying and thermal reduction modifications to synthesize the dielectric/magnetic multi-component $CoFe_2O_4$@N-rGO aerogel. The findings indicate that incorporating ethylene glycol (EG) as an organic solvent significantly mitigates the internal stress generated during the self-assembly process of graphene and $CoFe_2O_4$ into a gel, thereby preventing excessive volume shrinkage while successfully facilitating the formation of the $CoFe_2O_4$@N-rGO aerogel composite material. The substantial nitrogen doping enhances dipole polarization within graphene while establishing heterogeneous interfaces with $CoFe_2O_4$, thereby enhancing interfacial polarization. Furthermore, comparative studies reveal that the morphology of magnetic materials has a significant impact on the EMA performance of aerogels. In contrast to nanoparticles, high aspect ratio $CoFe_2O_4$ nanofibers demonstrate advantages in enhancing EMA performance even at low concentrations. Finally, structural disruption analyses of aerogels confirm that both macroscopic 3D continuous networks and cellular unit structures are key contributors to the exceptional EMA performance of GAs. Consequently, ingeniously designed and modified GAs exhibit characteristics such as low density, broad bandwidths, and strong absorption capabilities, making them promising candidates for lightweight and efficient EMA materials.

2 Experimental section

2.1 Materials

$Fe(NO_3)_3·9H_2O$ (AR), $Co(NO_3)_2·6H_2O$ (AR), urea (ACS reagent), and paraffin were obtained from J&K Scientific Co., Ltd. Polyvinylpyrrolidone (PVP, average M.W. 1,300,000) was supplied by Thermo Scientific. Ethylene glycol (AR) and N,N-dimethylformamide (DMF, GC) were obtained from Macklin Reagent Co., Ltd. Graphene oxide aqueous solution (GO, 4 mg/mL) was sourced from Hangzhou Hangdan Photoelectric Technology Co., Ltd.

2.2 Synthesis of $CoFe_2O_4$ nanofibers

$CoFe_2O_4$ nanofibers were synthesized using electrospinning combined with oxidation. First, 1 mmol of $Co(NO_3)_2{\cdot}6H_2O$ and 2 mmol of $Fe(NO_3)_3{\cdot}9H_2O$ were dissolved in 8 mL of DMF. Then, 1 g of PVP was added, and the mixture was magnetically stirred for 24 h to create a spinning solution. The spinning solution was then transferred to a syringe for electrostatic spinning. The electrospinning process involved applying a positive voltage of 16 kV and a negative voltage of –2 kV, with an injection speed of 0.2 mL/h. The spun nanofiber film was dried at 60 °C for 12 h. Finally, the dried nanofibers were subjected to oxidation in a muffle furnace. The heating process involved increasing the temperature to 500 °C at a rate of 2 °C/min and holding it for 2 h. After natural cooling, magnetic $CoFe_2O_4$ nanofibers were obtained.

2.3 Synthesis of $CoFe_2O_4$@N-rGO complex aerogel

The $CoFe_2O_4$@N-rGO composite aerogel was prepared using either $CoFe_2O_4$ nanofibers or 20 nm commercial $CoFe_2O_4$ nanoparticles as magnetic components. First, a 4 mg/mL aqueous solution of GO was diluted to a 2 mg/mL mixed solution using ethylene glycol. Then, 2.5 mg of $CoFe_2O_4$ nanofibers or nanoparticles were added to 5 mL of the mixed solution and ultrasonically dispersed for 1 h. Subsequently, 40 mg of urea was dissolved in the 5 mL $CoFe_2O_4$ dispersion, which was sealed in a 25 mL Teflon-lined stainless steel reactor and heat-treated at 160 °C for 2 h. At the end of the reaction, the EG in the resulting graphene solvent gel was replaced with water using the solvent exchange method. The graphene gel was then rapidly frozen with liquid nitrogen and vacuum freeze-dried to obtain the $CoFe_2O_4$@N-rGO composite aerogel. Finally, the composite aerogel was heated to 300 °C at a rate of 5 °C/min in a vacuum tube furnace and thermally reduced under a nitrogen atmosphere for 1 h. The obtained composite aerogel with $CoFe_2O_4$ nanofibers as the magnetic component was named NAG-Mf, while the composite aerogel with $CoFe_2O_4$ nanoparticles as the magnetic component was named NAG-Mp.

For comparison, the graphene aerogel PAG was prepared using the same process with a 2 mg/mL GO aqueous solution, without the addition of EG, urea, and magnetic components. The nitrogen-doped graphene aerogel (NAG) was also prepared using the same process, but without the addition of magnetic components.

2.4 Characterizations

Surface chemistry and structure were analyzed using X-ray photoelectron spectroscopy (XPS) (Thermo Scientific K-Alpha) and Fourier-transform infrared spectroscopy (FTIR) (Thermo Scientific Nicolet iS20). The crystal structure was analyzed using an X-ray diffractometer (Rigaku SmartLab SE) with Cu Kα radiation (λ = 0.154 nm). The magnetic properties were measured using a vibrating sample magnetometer (VSM) (LakeShore 7404). The morphology and structure were observed using scanning electron microscopy (SEM, TESCAN MIRA LMS), transmission electron microscopy (TEM, JEOL JEM F200), and energy-dispersive spectroscopy (EDS). Off-axis electron holography was conducted using a Lorentz transmission electron microscopy (JEOL JEM-2100F). The elemental contents of Co and Fe were determined by inductively coupled plasma optical emission spectrometry (ICP-OES). Sample size was measured using a digital display micrometer, sample mass was determined using an analytical balance, and sample density was calculated based on the sample's volume and weight. The filling amount of the sample in paraffin was calculated using the sample density and volume after mixing with paraffin, along with the total weight. To evaluate the EMA performance, aerogels were vacuum-impregnated with melted paraffin wax. The resultant mixture was then cut into concentric rings with an inner diameter of 3.04 mm and an outer diameter of 7.00 mm after solidification. The vector network analyzer (Agilent 5324A) was used to measure electromagnetic parameters in the frequency range of 2 to 18 GHz using the coaxial method.

3 Results and discussion

Figure 1(a) illustrates the preparation process of $CoFe_2O_4$ nanofiber@N-rGO composite aerogel (NAG-Mf). Firstly, $CoFe_2O_4$ nanofibers and GO were dispersed in a mixed solvent of water/EG to form a GO colloid solution using ultrasound. It is noteworthy that $CoFe_2O_4$ nanofibers are synthesized through a combination of electrospinning and oxidation techniques, with the corresponding SEM images presented in Figs. S1(a) and S1(b) in the Electronic Supplementary Material (ESM). Then, urea was dissolved in the GO colloid solution and subjected to a solvent-thermal reaction, during which GO sheets and $CoFe_2O_4$ nanofibers self-assembled into a hydrogel. Finally, the ethylene glycol in the hydrogel was replaced with water through solvent exchange and then freeze-dried to obtain nitrogen-doped $CoFe_2O_4$ nanofiber/N-rGO composite aerogel. Since the reduction effect of GO during the solvent-thermal process is limited, further reduction at 300 °C was carried out after aerogel preparation to enhance EMA performance. The presence of EG in the mixed solvent plays a crucial role in the self-assembly of $CoFe_2O_4$ and GO into graphene aerogels. Typically, when the GO colloidal solution undergoes hydrothermal or solvent-thermal reactions, significant gel volume shrinkage occurs, leading to the formation of stable graphene aerogels [22, 25]. However, dispersing $CoFe_2O_4$ in pure water as the solvent results in more severe volume shrinkage during the hydrothermal reaction, which causes gel cracking and reduces stability. As shown in Fig. S1(c) in the ESM, contrast samples (CNAG-Mp and CNAG-Mf) prepared with water as the solvent exhibited significant volume shrinkage and fragmentation phenomena. After changing the solvent to a mixture of water/EG, the prepared NAG-Mp and NAG-Mf showed similar volumes to PAG and NAG without experiencing severe volume shrinkage. SEM images (Figs. S1(d)–S1(g) in the ESM) revealed that, compared with NAG-Mf/Mp, CNAG-Mf/Mp had smaller cellular unit structures within their respective graphene aerogels. The addition of urea to the GO solution not only caused the restacking of graphene sheets into a 3D structure under van der Waals forces but also led to nucleophilic substitution reactions with nitrogen-containing substances [26]. The XPS spectra in Fig. 1(b) showed noticeable N 1s peaks for nitrogen-doped samples, while no peak was observed for the non-nitrogen-doped PAG aerogel. The high-resolution XPS spectrum for N 1s on NAG-Mf confirmed that doped-N mainly existed as pyridinic-N, pyrrolic-N, and graphitic-N forms, with pyrrolic-N being predominant. Additionally, different morphologies of $CoFe_2O_4$ were incorporated into NAG-Mf/Mp, resulting in distinct peaks for Co 2p and Fe 2p on the XPS spectra (Fig. 1(b)). The high-resolution Co 2p spectrum (Fig. 1(d)) has been deconvoluted into four distinct peaks located at approximately 780.2, 787.4, 795.9, and 803.2 eV. Among these, the peaks centered at around 780.2 and 795.9 eV correspond to the Co $2p_{3/2}$ and Co $2p_{1/2}$ states, respectively, while the remaining two peaks represent spin-orbit splitting features [27]. In the Fe 2p spectrum (Fig. 1(e)), two main peaks of Fe $2p_{3/2}$ and Fe $2p_{1/2}$ appear at approximately

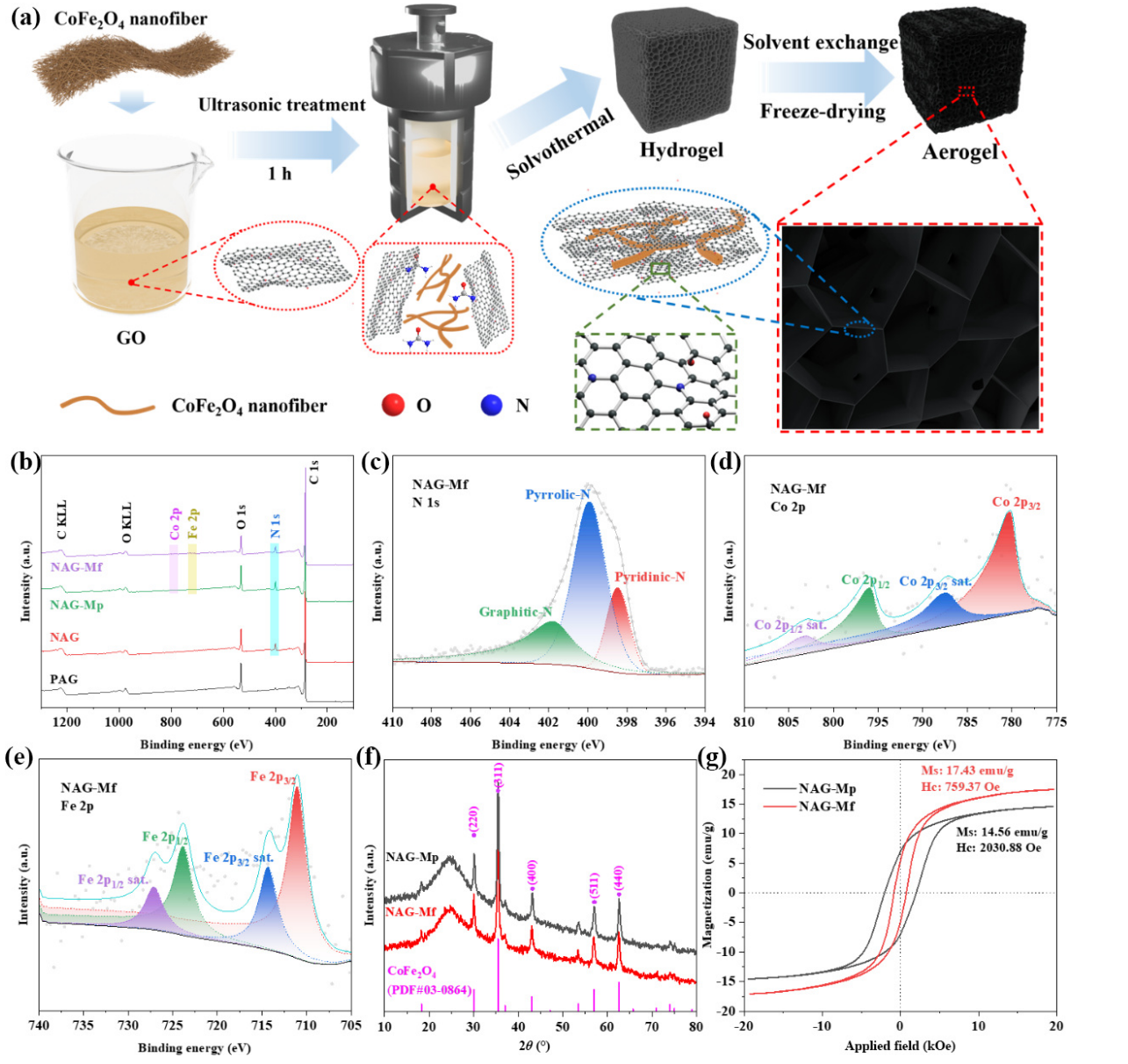

Figure 1 (a) Schematic diagram illustrating the preparation process of $CoFe_2O_4$ nanofiber@N-rGO composite aerogels. (b) XPS spectra of PAG, NAG, NAG-Mp, and NAG-Mf aerogels. High-resolution XPS spectra of (c) N 1s, (d) Co 2p, and (e) Fe 2p for the NAG-Mf aerogel. (f) XRD patterns of NAG-Mp and NAG-Mf aerogels. (g) Hysteresis loops measured at room temperature.

711.0 and 724.1 eV. Additionally, the two peaks near 714.3 and 727.1 eV represent split peaks of the spin-orbit orbits. The difference in binding energies between the main peaks is approximately 13.8 eV, suggesting that Fe is present in a trivalent oxidation state, consistent with the standard spinel structure of $CoFe_2O_4$ [28, 29]. The XRD patterns confirmed the well-defined crystalline spinel structure of $CoFe_2O_4$ nanofibers in NAG-Mf, as depicted in Fig. 1(f). Both NAG-Mf and NAG-Mp exhibited similar diffraction peak positions at 30.063°, 35.451°, 43.472°, 57.166°, and 62.726°, corresponding to prominent diffraction peaks assigned to the (220), (311), (400), (511), and (440) planes, respectively, for $CoFe_2O_4$ according to the JCPDF standard card No. 030864. This indicates that the prepared $CoFe_2O_4$ nanofibers and commercial $CoFe_2O_4$ nanoparticles both possess crystalline spinel structures. Magnetically-active antiferrospinel-type $CoFe_2O_4$ has been shown to exhibit favorable magnetic loss properties, effectively adjusting the impedance matching of EMA materials [30]. The hysteresis loop (Fig. 1(g)) illustrates the influence of $CoFe_2O_4$ morphology on its magnetic properties, with NAG-Mf aerogel demonstrating higher saturation magnetization and lower coercivity under comparable $CoFe_2O_4$ content (Table S1 in the ESM). This suggests that the nanofiber morphology of $CoFe_2O_4$ in NAG-Mf enhances its magnetic response, making it more efficient for applications that demand high magnetic loss and optimized EMA performance.

The microstructure of aerogels was examined through SEM and TEM. The SEM image in Fig. 2(a) reveals that the NAG is composed of stacked rGO sheets in a 3D structure, forming a cell-unit structure with the rGO sheets acting as cell walls. The structures of NAG-Mp and NAG-Mf aerogels are similar to NAG, primarily composed of rGO-based cell-unit structures. However, upon magnification of the cell wall, it is evident that $CoFe_2O_4$ nanoparticles or nanofibers are encapsulated within them (Figs.

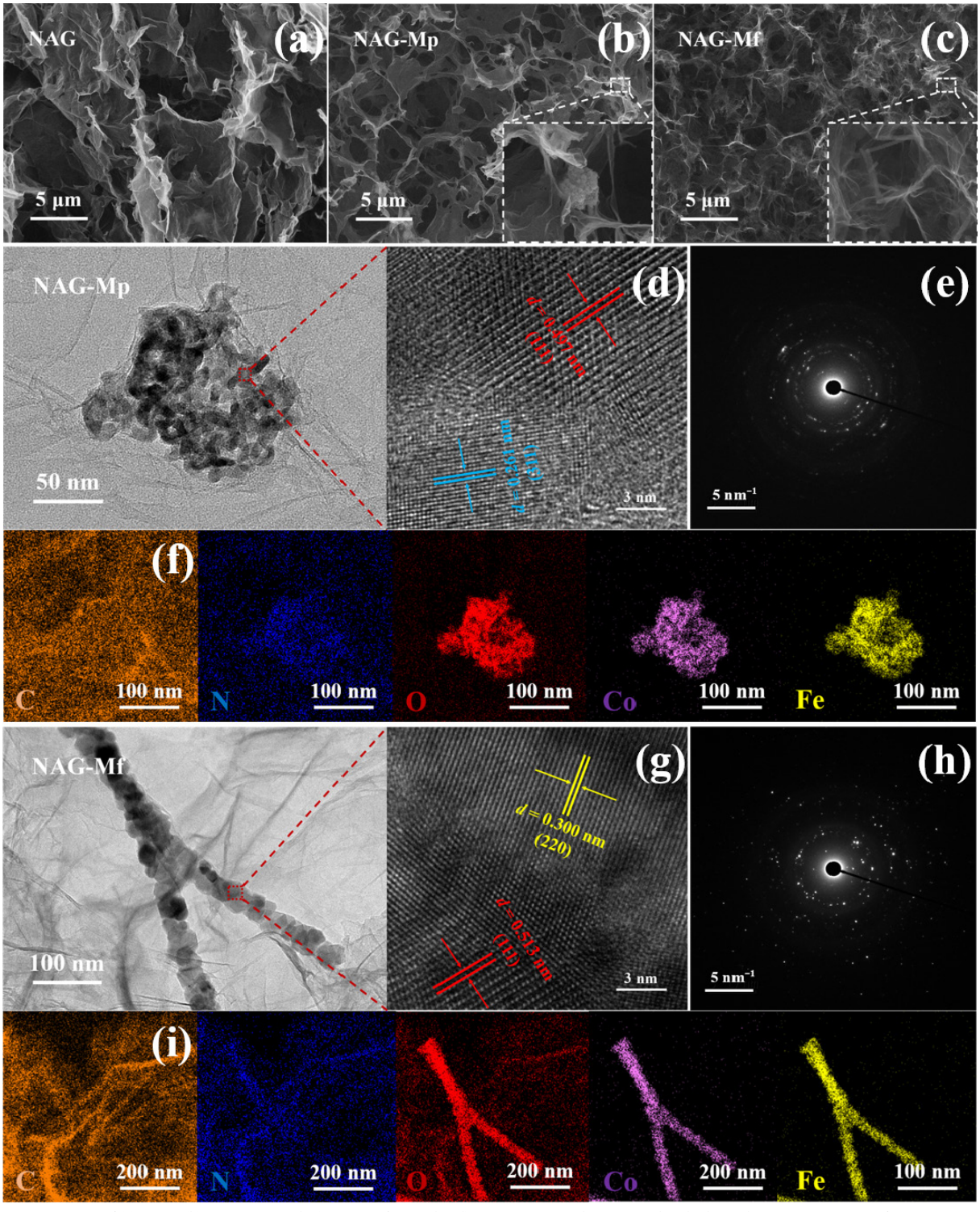

Figure 2 SEM images of (a) NAG, (b) NAG-Mp, and (c) NAG-Mf aerogels. (d) TEM images and corresponding high-resolution TME images of NAG-Mp aerogel. (e) Selected area electron diffraction (SAED) pattern of NAG-Mp aerogel. (f) Element mapping images of NAG-Mp aerogel. (g) TEM and corresponding high-resolution TME images of NAG-Mf aerogel. (h) SAED pattern of NAG-Mf aerogel. (i) Element mapping images of NAG-Mf aerogel.

2(b) and 2(c), and inset). Although the $CoFe_2O_4$ nanoparticles have a diameter of 20 nm, unavoidable aggregation into larger particles during the aerogel preparation process affects the magnetic field distribution in the absorber material. Due to their high aspect ratio, $CoFe_2O_4$ nanofibers are less likely to aggregate into larger particles and also provide support to mitigate the tendency for 2D stacking of rGO sheets (Fig. 2(c) inset). TEM further confirms the composite architecture of $CoFe_2O_4$ integrated with rGO. Figures 2(d) and 2(g) illustrate that $CoFe_2O_4$ nanoparticles and nanofibers are either dispersed or encapsulated within rGO sheets, resulting in the formation of heterostructures. High-resolution TEM analysis reveals lattice fringes corresponding to the (111), (220), and (311)

crystal planes of $CoFe_2O_4$ on both nanoparticles and nanofibers, which are also distinctly observable in their respective electron diffraction patterns. Finally, TEM elemental mappings (Figs. 2(f) and 2(i)) demonstrate that both nanoparticles and nanofibers are composed of Co, Fe, and O elements. This confirms that the $CoFe_2O_4$ nanofiber@N-rGO aerogel is indeed a composite of $CoFe_2O_4$ nanofibers on graphene. Furthermore, the abundant presence of nitrogen on rGO sheets confirms successful doping with nitrogen atoms.

Based on the above, the self-assembly behavior of GO and $CoFe_2O_4$ nanofibers/particles during the hydrothermal process can be inferred. Firstly, due to ultrasonic dispersion in the mixed solvent, $CoFe_2O_4$ nanofibers/particles and GO form stable colloidal solutions, with strong electrostatic repulsion generated by the ionization of hydrophilic oxygen-containing groups (such as hydroxyl, carboxyl, and epoxy functional groups), which overcome van der Waals forces on the carbon skeleton [31]. The $CoFe_2O_4$ nanoparticles inevitably aggregate into larger particles due to their small size and large surface energy. As the temperature increases during the solvent-thermal reaction, the oxygen-containing groups in GO are reduced and eliminated, enhancing the π–π conjugated structure of the rGO sheets while weakening electrostatic repulsion. When van der Waals forces exceed electrostatic repulsion, rGO sheets tend to restack into a 3D structure. $CoFe_2O_4$ nanofibers and particles are dispersed on the surface of rGO sheets or are partially covered by the 2D stacked rGO sheets. This results in the formation of numerous heterojunction interfaces between $CoFe_2O_4$ nanofibers/particles and rGO, which enhances the interface polarization loss capability. Due to the decreased surface charge and increased hydrophobicity resulting from the hydrothermal or solvent-thermal process, the formed gels exhibit significant volume shrinkage compared to the initial volume of the GO colloidal solution. This effect is especially pronounced when dispersing $CoFe_2O_4$ nanofibers/particles in the GO colloid solution, leading to further shrinkage of the resulting graphene gel and compromising its stability.

To explore the role of mixed solvents in mitigating volume shrinkage in aerogels, the functional group changes on graphene in the aerogel were studied. The C 1s fine spectra of PAG, NAG, NAG-Mp, and NAG-Mf (Figs. S2(a)–S2(d) in the ESM) primarily show peaks related to C–C/C=C, C–O, and O–C=O bonds. Additionally, nitrogen doping of NAG, NAG-Mp, and NAG-Mf aerogels resulted in the observation of a C–N peak. The O 1s fine spectra (Figs. S2(e)–S2(h) in the ESM) indicate that PAG, NAG, NAG-Mp, and NAG-Mf predominantly contain C–O, O=C–OH, and –OH groups. Furthermore, the integration of $CoFe_2O_4$ into the NAG-Mp and NAG-Mf aerogels synthesized with mixed solvents led to an enhanced O–Co/Fe peak. Moreover, it was observed that compared to the PAG aerogel prepared using water as the solvent, the proportion of O=C–OH and –OH groups slightly increased in the aerogel prepared with mixed solvents. As shown in Fig. S2(i) in the ESM, compared to the control samples PAG, CNAG-Mp, and CNAG-Mf, the aerogels prepared with mixed solvents NAG, NAG-Mp, and NAG-Mf, exhibited enhanced peaks at 1140 and 940 cm^{-1}. Combined with the increase of O=C–OH and –OH in the fine spectrum of O 1s in XPS, it can be inferred that the peak at 1140 cm^{-1} is attributed to C–O stretching vibration in –COOH, while the peak at 940 cm^{-1} is attributed to the bending vibration of –OH in –COOH. The combination of XPS and FTIR suggests that EG in mixed solvents enables aerogels to retain more –COOH. Due to its strong ionization ability, it enhances charge interactions between graphene sheets, allowing it to counteract excessive van der Waals forces, thus preventing volume shrinkage during gel formation caused by adding $CoFe_2O_4$. Ultimately, this mitigates issues of excessive gel contraction and instability.

To assess the EMA performance of GA-based materials and examine the effect of $CoFe_2O_4$ morphology on EMA performance, the reflection loss (RL) at specific frequencies and thicknesses was calculated using transmission line theory. This calculation was derived from the relative dielectric permittivity ($\varepsilon_r = \varepsilon' - j\varepsilon''$) and the relative magnetic permeability ($\mu_r = \mu' - j\mu''$) [32–34].

$$Z_{in} = Z_0\sqrt{\frac{\mu_r}{\varepsilon_r}}\tanh\left(j\frac{2\pi fd\sqrt{\mu_r\varepsilon_r}}{c}\right) \quad (1)$$

$$RL = 20\log_{10}\left|\frac{Z_{in} - Z_0}{Z_{in} + Z_0}\right| \quad (2)$$

Here, Z_0 represents the free space impedance, Z_{in} is the input impedance of the absorber, c denotes the speed of light, and d refers to the thickness of the absorber. In general, RL ≤ –10 dB indicates that the absorption of electromagnetic waves by the absorber exceeds 90%, and the corresponding bandwidth is known as the EAB [35, 36]. The EMA characteristics of GAs in the frequency range of 2 to 18 GHz were calculated using Eqs. (1) and (2), along with a metal base plate model (Figs. 3(a)–3(d)). The unmodified GA (PAG aerogel) exhibits commendable EMA performance, with a maximum effective absorption bandwidth (EAB) reaching a noteworthy 8.0 GHz. However, the maximum absorption intensity reaches only –24.9 dB at a thickness of 2.5 mm (Fig. 3(a)). The maximum absorption for N-doped GA (NAG aerogel) increases slightly, reaching –31.4 dB at a thickness of 2.6 mm, as shown in Fig. 3(b). The enhanced performance of NAG aerogel can be attributed to doped nitrogen atoms, which disrupt the sp^2 hybridization of the graphene hexagonal lattice, forming numerous dipole polarization centers and enhancing the material's dipole polarization loss ability. To further improve EMA performance, NAG-Mp and NAG-Mf composite aerogels were prepared by incorporating magnetic material $CoFe_2O_4$ into N-doped GA. $CoFe_2O_4$ provides both a magnetic loss path for GA and introduces a heterostructure that enhances interface polarization loss. Although the morphology of $CoFe_2O_4$ in NAG-Mp and NAG-Mf differs only slightly, the impact on EMA performance enhancement is substantially different. In comparison to NAG aerogels, the absorption strength of NAG-Mp aerogels increased to –34.5 dB, while the EAB remained essentially unchanged (Fig. 3(c)). In contrast, the EMA performance of NAG-Mf aerogel was greatly enhanced, reaching –53.5 dB at a thickness of 2.7 mm. Furthermore, the maximum achievable EAB for NAG-Mf was extended to 8.7 GHz, indicating significant improvements in performance. In conclusion, the microstructures designed within NAG-Mf aerogel play a crucial role in enhancing EMA properties, resulting in superior performance. The improved EMA properties confirm the presence of functional structures that contribute to electromagnetic wave loss.

To further explore the influence of various aerogel structures on the performance of EMA, impedance matching, relative permittivity, relative permeability, and the corresponding loss tangents ($\tan\delta_\varepsilon = \varepsilon''/\varepsilon'$, $\tan\delta_\mu = \mu''/\mu'$) were examined to elucidate the enhanced EMA performance of NAG-Mf aerogel. Impedance matching is crucial for ensuring electromagnetic wave penetration

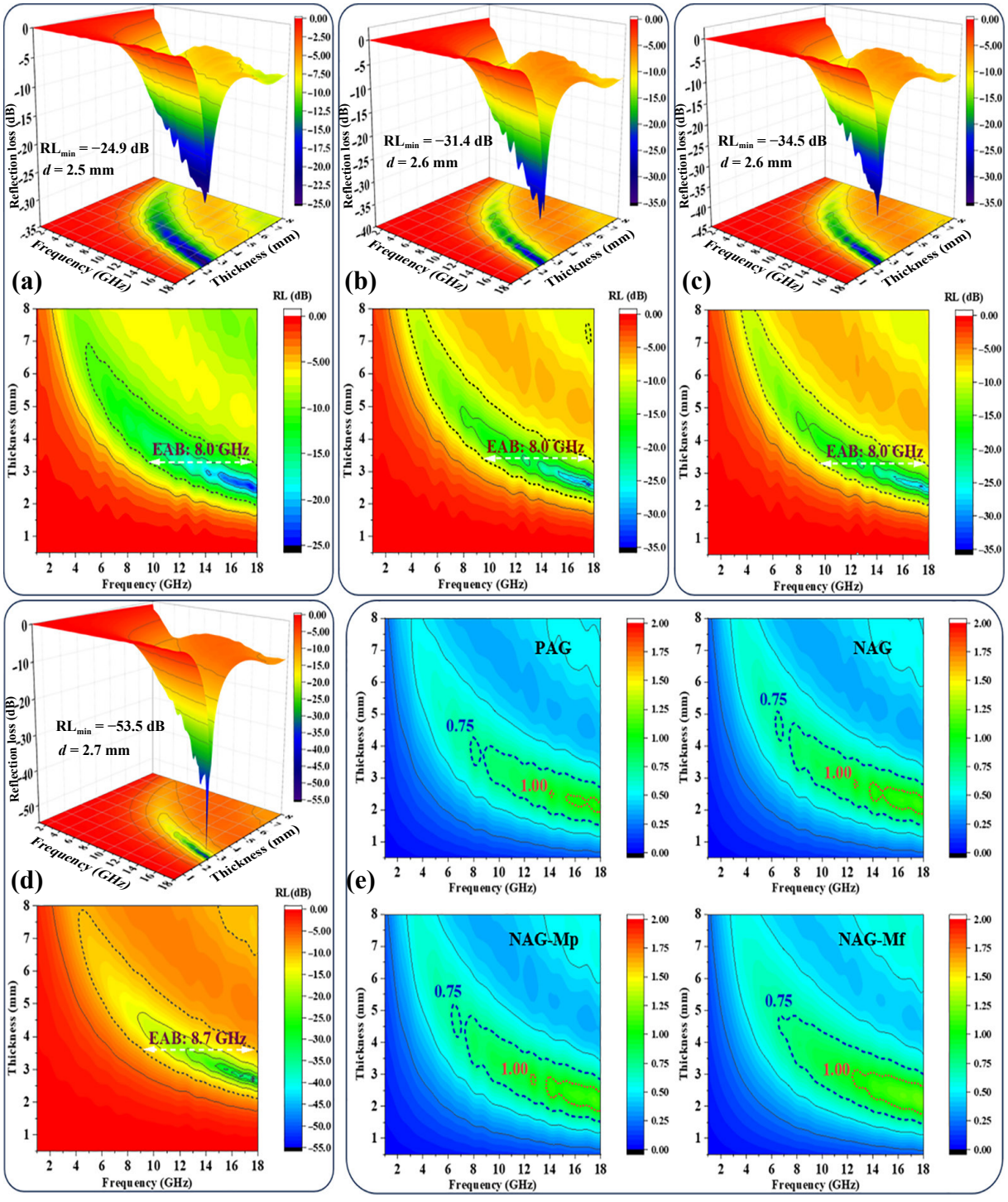

Figure 3 3D RL–*f* images with 2D plane views of (a) PAG, (b) NAG, (c) NAG-Mp, and (d) NAG-Mf aerogels. (e) 2D impedance matching contour map.

into the EMA material. When the impedance matching coefficient $Z = Z_{in}/Z_0 = 1$, the material's impedance aligns with that of free space, allowing all electromagnetic waves to enter without reflection [37]. The dissipation of these electromagnetic waves occurs through diverse loss mechanisms enabled by the material's unique functional structure, thereby completing the EMA process. Figure 3(e) illustrates the impedance matching of PAG, NAG, NAG-MP, and NAG-MF aerogels. In the high-frequency region (15.2–18.0 GHz), PAG aerogel demonstrates excellent impedance matching, allowing the penetration of electromagnetic waves and their dissipation through dipole polarization loss mechanisms facilitated by residual oxygen-containing groups and lattice defects on the rGO sheet. Moreover, rGO's superior electrical conductivity enhances the dissipation of electromagnetic waves via conductive loss. Thus, PAG aerogel exhibits superior EMA performance in the high-frequency region. The impedance matching region (13.7–18.0 GHz) of NAG aerogel exceeds that of PAG, demonstrating that nitrogen doping further enhances impedance matching. Additionally, nitrogen doping significantly improves the dipole polarization capability of rGO in NAG aerogel, thereby enhancing

its EMA performance. While the incorporation of $CoFe_2O_4$ nanoparticles into NAG-Mp aerogel maintains an excellent impedance matching region (13.5–18.0 GHz), the improvement in EMA performance is not significant. This can be attributed to the low quantity of $CoFe_2O_4$ and the severe agglomeration of nanoparticles, which restrict the magnetic field range and the formation of heterogeneous interfaces, thereby weakening magnetic loss and interface polarization loss. By contrast, incorporating $CoFe_2O_4$ nanofibers in NAG-Mf aerogel resolves the agglomeration issue, increases the formation of heterogeneous interfaces, optimizes impedance matching (12.0–18.0 GHz), and enhances interfacial polarization, leading to significantly improved EMA performance. Electromagnetic parameters further confirmed enhanced EMA performance in the NAG-Mf aerogel. The nitrogen doping strategy and the incorporation of $CoFe_2O_4$ were observed to reduce both the real and imaginary parts of the dielectric constants of NAG, NAG-MP, and NAG-MF aerogels (Figs. S3(a) and S3(b) in the ESM). This optimization, however, improved the materials' impedance matching characteristics. Additionally, the electrical loss tangent $\tan\delta_\varepsilon$ of NAG-Mf was significantly higher than that of other aerogels (Fig. S3(c) in the ESM), indicating enhanced electromagnetic wave attenuation in NAG-Mf aerogels. While PAG aerogel also exhibited a high electrical loss tangent, poor impedance matching led to the direct reflection of electromagnetic waves, deteriorating its EMA performance. It is important to note that the reflection of electromagnetic waves is influenced by ε_r/μ_r, highlighting the importance of incorporating magnetic components to further enhance electromagnetic performance. The inclusion of magnetic $CoFe_2O_4$ optimized impedance matching, particularly for NAG-Mf aerogel, which demonstrated a larger impedance matching region and broadened EAB. Moreover, variations in relative permeability revealed that the morphology of $CoFe_2O_4$ within the aerogel significantly influenced its magnetic properties. As shown in Fig. S3(d) in the ESM, $CoFe_2O_4$ nanofibers notably enhanced both the real and imaginary parts, as well as the tangent magnetic loss associated with relative permeability in NAG-Mf aerogel. In contrast, the $CoFe_2O_4$ nanoparticles in NAG-Mp aerogel showed no significant change in relative permeability (Figs. S3(d)–S3(f) in the ESM), reflecting their limited effect.

The relative dielectric constant (ε) is primarily associated with polarization relaxation in aerogels. According to Debye relaxation theory, the Cole–Cole semicircle describes the polarization relaxation in EMA processes. The relationship between ε' and ε'' is described by the following Eq. (3) [38–40]

$$(\varepsilon' - \frac{\varepsilon_s - \varepsilon_\infty}{2})^2 + (\varepsilon_p'')^2 = (\frac{\varepsilon_s - \varepsilon_\infty}{2}) \quad (3)$$

where ε_∞ is the relative dielectric constant in the high-frequency limit, ε_s is the static dielectric constant, and ε_p" is the imaginary part of the relative complex dielectric constant caused by dielectric polarization. In the Cole–Cole curves, each Cole–Cole semicircle corresponds to a Debye relaxation process. In the absence of an obvious semicircle, it can be considered that the dielectric loss mainly arises from conductivity loss, which can be expressed by the following Eq. (4)

$$\varepsilon_c'' = \frac{\sigma}{\varepsilon_0 \omega} \quad (4)$$

where ε_c" is the imaginary part of the relative dielectric constant caused by conductivity loss; σ is electrical conductivity; and ω is the angular frequency.

A significant number of defects and residual oxygen-containing groups exist in the rGO of PAG aerogel. These defects act as centers of dipole polarization, leading to dipole polarization relaxation during the EMA process. NAG aerogels, doped with nitrogen atoms on rGO, introduce additional dipole polarization centers, further enhancing dipole polarization relaxation. Furthermore, $CoFe_2O_4$ nanoparticles and nanofibers were incorporated into NAG-Mp and NAG-Mf aerogels, respectively, resulting in charge accumulation at the heterogeneous interface between $CoFe_2O_4$ and rGO during EMA, leading to interfacial polarization relaxation. In summary, PAG, NAG, NAG-MP, and NAG-MF aerogels exhibit multiple types of polarization relaxation losses during the EMA process. Consequently, the Cole–Cole curves (Figs. 4(a)–4(d)) consist of multiple semicircles. Additionally, the excellent electrical conductivity contributes to conductivity loss, represented by a long straight tail in the Cole–Cole curves.

The magnetic material $CoFe_2O_4$ has been incorporated into NAG-Mp and NAG-Mf aerogels to introduce magnetic loss mechanisms. However, the relative permeability of NAG-Mp aerogel did not show significant changes, possibly due to the limited amount of $CoFe_2O_4$ and severe agglomeration of nanoparticles, which restricted its magnetic properties. Conversely, although a comparable quantity of $CoFe_2O_4$ was incorporated into the NAG-Mf aerogel (Table S1 in the ESM), there was a marked enhancement in magnetic loss capacity and notable changes in relative permeability. This phenomenon can be ascribed to the presence of $CoFe_2O_4$ nanofibers within the NAG-Mf aerogel, which alleviates the issue of excessive nanoparticle aggregation. This enhancement broadens the distribution of magnetic components within the aerogel, thereby significantly increasing the probability of interactions with electromagnetic waves. Furthermore, intrinsic magnetic field lines between adjacent magnetic nanofibers led to magnetic coupling effects, enhancing the range and strength of the magnetic field. The hysteresis loop (Fig. 1(g)) demonstrated a larger saturation magnetization for NAG-Mf aerogel. Off-axis electron holography provides verification of the magnetic coupling phenomenon. As illustrated in Fig. 4(e), the magnetic currents emitted by neighboring $CoFe_2O_4$ nanofibers interact to establish a high-density three-dimensional magnetic coupling network within the NAG-Mf aerogel. This phenomenon effectively enhances the magnetic loss capability in non-magnetic regions. Therefore, although NAG-Mf aerogel and NAG-Mp differ only in the $CoFe_2O_4$ morphology, the magnetic properties have been significantly improved.

Magnetic loss occurs as a result of the interaction between magnetic materials and alternating electromagnetic fields. It has been reported that magnetic loss in the frequency range of 2–18 GHz is primarily influenced by natural resonance, exchange resonance, eddy current loss, and magnetic coupling effects. Natural resonances typically occur within the 2–10 GHz range, while exchange resonances are more common at higher frequencies (> 10 GHz). Eddy current loss can be quantified using the following Eq. (5) [41]

$$C_0 = \frac{\mu''}{\mu'^2 f} = \frac{2}{3}\pi\mu_0 d^2\sigma \quad (5)$$

where μ_0 represents the vacuum permeability, σ is the conductivity of the composite material, and d denotes the matching thickness. When C_0 remains constant across different frequencies, eddy current loss is identified as the primary mechanism for magnetic loss in the composite. As depicted in Fig. 4(f), NAG-Mf aerogel

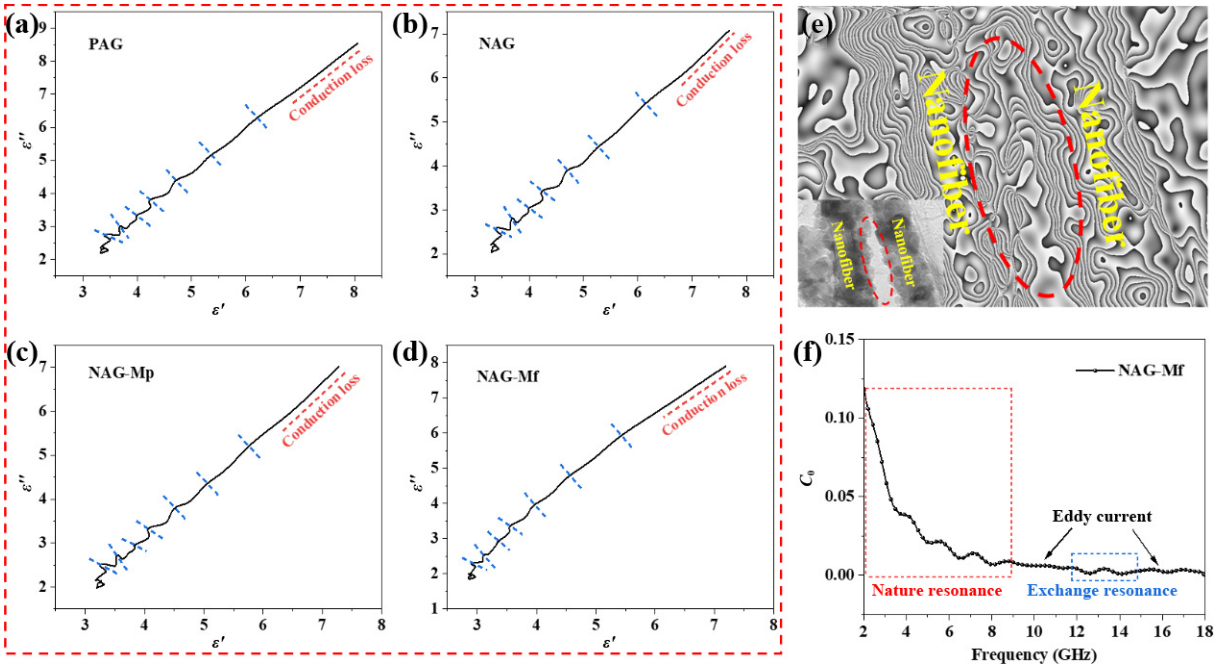

Figure 4 Cole–Cole curves (ε'–ε'' plots) for (a) PAG, (b) NAG, (c) NAG-Mp, and (d) NAG-Mf aerogels. (e) Off-axis electron holography image between two neighbor $CoFe_2O_4$ nanofibers with an inset corresponding to the TEM image. (f) C_0–f curve of NAG-Mf aerogel.

displayed fluctuations in C_0 due to natural resonance and exchange resonance at low frequencies (2.0–8.5 GHz) and high frequencies (11.8–14.9 GHz), respectively, while remaining relatively constant within other frequency bands (8.5–11.8 and 14.9–18.0 GHz). This indicates that magnetic loss within these constant bands is primarily due to eddy current loss.

In general, the electromagnetic wave attenuation capacity of EMA materials is typically evaluated using the attenuation constant (α), which is expressed as follows Eq. (6) [42, 43]

$$\alpha = \frac{\sqrt{2}\pi f}{c} \times \sqrt{(\mu_y''\varepsilon_y'' - \mu_y'\varepsilon_y') + \sqrt{(\mu_y''\varepsilon_y'' - \mu_y'\varepsilon_y')^2 + (\mu_y'\varepsilon_y'' + \mu_y''\varepsilon_y')^2}} \quad (6)$$

The attenuation constant derived from electromagnetic parameters is shown in Fig. S4 in the ESM. The PAG aerogel exhibits a high attenuation constant, indicating a strong capacity for attenuating electromagnetic waves. However, its poor impedance matching ultimately limits its EMA performance. These observations suggest that a high attenuation capability alone is insufficient for achieving optimal EMA performance; optimal impedance matching must also be considered. The attenuation constants of the NAG and NAG-MP aerogels are slightly lower than that of PAG, but their improved EMA performance is primarily attributed to optimized impedance matching. In contrast, the NAG-Mf aerogel exhibits a high attenuation constant comparable to that of PAG, but with superior impedance matching, leading to a substantial improvement in EMA performance. This also highlights the advantages of magnetic $CoFe_2O_4$ nanofibers over nanoparticles, as they achieve greater enhancement in performance with less magnetic material addition.

To further investigate the EMA properties of NAG-Mf aerogel, the relationship between the position of RL_{min} and thickness was examined. It was observed that the relationship strongly correlates with the one-quarter wavelength (1/4λ) cancellation theory. Specifically, when the absorber thickness d_m is an odd multiple of 1/4λ of the electromagnetic wave, as described by the following formula, the optical path difference between the incident wave and the reflected wave becomes an odd multiple of one-half wavelength, resulting in interference cancellation [44]

$$d_m = \frac{n\lambda}{4} = \frac{nc}{4f_m\sqrt{\varepsilon_r\mu_r}} \quad (n = 1, 3, 5, 7, \ldots) \quad (7)$$

As shown in Fig. S5 in the ESM, the experimental values of d_m and 1/4λ are largely consistent, indicating the presence of interference loss in NAG-Mf aerogel.

In order to investigate the impact of aerogel structure on EMA properties, the NAG-Mf aerogel was crushed and subsequently mixed with a paraffin matrix in the same concentration as the original NAG-Mf aerogel for EMA measurements. As demonstrated in Fig. S6(a) in the ESM, the microstructural disruption caused the NAG-Mf aerogel to lose its continuous 3D network structure and the rGO-based cell units, reducing them to flat particles. These particles were incapable of forming a continuous electron conduction pathway within the paraffin matrix, especially at very low filler concentrations. Additionally, the destruction of the cell structure significantly weakened the multiple reflections and scattering of electromagnetic waves on the rGO cell walls, diminishing the likelihood of interaction between the incident electromagnetic waves and the functional structures. To determine the filling fraction of the NAG-Mf aerogel in the paraffin matrix, the density of the NAG-Mf aerogel (approximately 7 mg/cm^3) was determined through mass and volume measurements, and the precise filling fraction (approximately 0.8%) was calculated accordingly. The RL of the disrupted NAG-Mf aerogel powder, under the same filling fraction, is depicted in Fig. S6(b) in the ESM, showing negligible EMA performance. Thus, both the continuous three-dimensional network and the intact cell units are essential for optimizing the EMA performance of NAG-Mf aerogels.

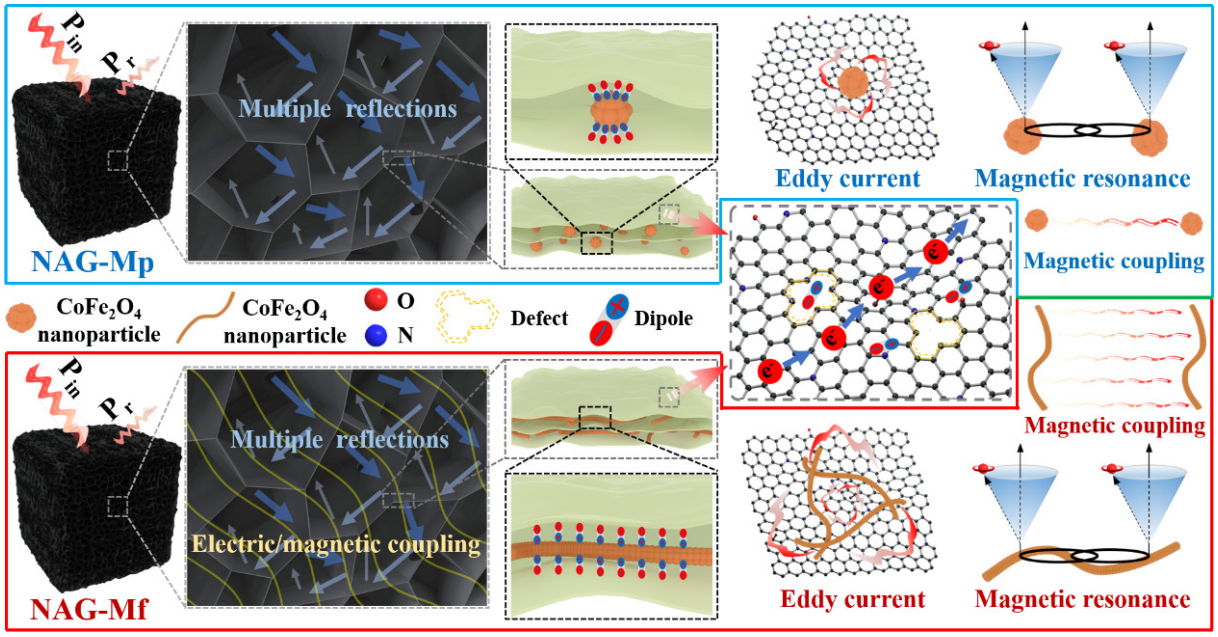

Figure 5 Schematic illustrations of the EMA mechanism.

Based on the preceding discussion, the interaction mechanism between the $CoFe_2O_4$@GA composite aerogel and electromagnetic waves is summarized. As depicted in Fig. 5, at the macro level, when electromagnetic waves are incident on the NAG-Mf or NAG-Mp aerogel, most waves penetrate the material directly due to excellent impedance matching, rather than reflecting off the surface. Electromagnetic waves entering the aerogels are captured by the cell structure of the aerogels, and multiple reflections occur on the cell walls composed of rGO sheets, greatly increasing the probability of interaction between the electromagnetic waves and functional structures. The strong magnetic coupling effect demonstrated by $CoFe_2O_4$ nanofibers in NAG-Mf aerogel significantly extends the magnetic field range and establishes a 3D electrical/magnetic coupling network when interacting with incident electromagnetic waves. As a result, this further enhances their capability to capture and attenuate electromagnetic waves [45]. At the microscopic level, both NAG-Mf and NAG-Mp aerogels feature multilayer cell walls composed of rGO sheets and magnetic $CoFe_2O_4$. The rGO sheets exhibit high electrical conductivity, and their interconnected structure forms a continuous three-dimensional conductive network. Under the influence of electromagnetic fields, electrons move and transition within the conductive network, resulting in substantial Joule heating, converting electromagnetic energy into thermal energy, and promoting conductivity loss [37, 46]. The inherent defects and residual oxygen-containing groups on the surface of rGO serve as dipole polarization centers, enhancing polarization loss. In addition, because of the high electronegativity of nitrogen atoms, the nitrogen dopant in graphene facilitates the generation and oscillation of dipoles, thereby enhancing the polarization loss ability [47]. The layered structure of the cell wall results in a heterogeneous interface between rGO and $CoFe_2O_4$. Because of the difference in Fermi levels among the various components, electrons are shifted to reach the equilibrium Fermi level, and the redistributed charge in this process becomes trapped at the interface, leading to significant interfacial polarization [47]. When external electromagnetic energy disrupts the charge balance at the interface, to restore equilibrium, the charge is transferred and transformed in a directional manner on the surface, forming a stable transition zone [46]. At this time, the interface polarization dissipates a significant amount of electromagnetic energy. In NAG-Mp aerogels, severe agglomeration of $CoFe_2O_4$ nanoparticles diminishes the contact area between $CoFe_2O_4$ and graphene, limits the formation of heterogeneous interfaces, and thereby diminishes the interface polarization loss ability. Conversely, in NAG-Mf aerogels, $CoFe_2O_4$ nanofibers prevented excessive aggregation and enhanced their dispersion in the graphene layered structures, facilitating the formation of heterogeneous interfaces. Furthermore, highly dispersed $CoFe_2O_4$ nanofibers provide substantial benefits in augmenting eddy current loss, magnetic resonance, and magnetic coupling. Eddy current loss and magnetic resonance depend on the interaction between magnetic components and electromagnetic waves, and $CoFe_2O_4$ nanofibers with enhanced dispersion properties extend the interaction range between magnetic components and electromagnetic waves. Therefore, the $CoFe_2O_4$ nanofibers in NAG-Mf aerogel are particularly effective in enhancing eddy current loss and magnetic resonance. Additionally, the effective dispersion of $CoFe_2O_4$ nanofibers reduces the average distance between magnetic materials, enhances the magnetic coupling effect, and increases the spatial range of the magnetic coupling network. In contrast, the agglomeration of $CoFe_2O_4$ nanoparticles increases the distance between magnetic materials, weakening the magnetic coupling effect and making it difficult for agglomerated nanoparticles to form extensive magnetic coupling networks. In conclusion, compared to $CoFe_2O_4$ nanoparticles, $CoFe_2O_4$ nanofibers greatly enhance EMA properties in NAG-Mf aerogel with a minimal amount of addition, despite only undergoing morphological changes.

An increased filling content results in higher weight and costs associated with EMA materials in practical applications. Therefore, achieving excellent performance with a minimal filling amount is a primary objective of advanced EMA materials. Aerogel materials are among the most promising EMA materials for achieving ultra-low filling capacities due to their lightweight characteristics. In this

study, the performance of EMA has been significantly enhanced through a stepwise design improvement of graphene aerogel. Notably, at extremely low fill content, NAG-Mf demonstrates an impressive ultra-wide EAB. To emphasize the advantages of NAG-Mf, we present comparative tables of graphene aerogel composites reported in recent years (Table 1). NAG-Mf achieves an ultra-low filling amount (~ 0.8%) due to its adoption of monolithic paraffin impregnation, which preserves the macroscopic structure of the aerogel. This amount is significantly lower than that of most reported graphene aerogel composites. Furthermore, the maximum EAB of NAG-Mf aerogel reached 8.7 GHz, surpassing that of most EMA materials. Consequently, NAG-Mf fully exploits the advantages of graphene aerogel, achieving an ultra-wide EAB at an ultra-low filling content.

Table 1 Comparison of the maximum EAB of some previously reported graphene aerogel composites

Sample	Filler loading (wt.%)	RL_{min} (dB)	EAB_{max} (GHz)	Density (mg/cm^3)	Refs.
NrGO/Co-MnO aerogel	20	−51.7	4.08	—[a]	[48]
PI/rGO/CNC-1 aerogel	5	−75.0	7.28	9.93	[49]
$MAPbI_3$/rGO aerogel	15	−64.35	6.4	7.69	[50]
Ni@TiO_2/MXene/rGO aerogel	5	−71.4	6.48	5.58	[51]
SiO_2/rGO/Co aerogel	—	−69.2	7.51	4.3	[52]
PI-$GP_{1/3}$-rGO aerogel	85	−32.9	6.22	63.7	[53]
$CoFe_2O_4$/N-rGO aerogel	20	−60.4	6.48	—	[17]
LAS@RGO/$CoFe_2O_4$ aerogel	23.1	−50.0	6.16	—	[54]
NAG-Mf aerogel	~ 0.8	−53.5	8.7	~ 7	This work

[a] Unclear.

4 Conclusions

Through the process of electrospinning, $CoFe_2O_4$ nanofibers were prepared and subsequently incorporated as magnetic components into nitrogen-doped graphene aerogel to fabricate a NAG-Mf composite aerogel with superior EMA properties. The $CoFe_2O_4$ nanofibers are coated with rGO sheets, forming an interconnected multi-layer structure that creates a 3D network. The high aspect ratio of the nanofibers compensates for the limitations of nanoparticles in terms of heterointerface polarization, eddy current loss, magnetic resonance, and magnetic coupling within the composite aerogel. This significantly enhances EMA performance, even at low addition levels. At a thickness of 2.7 mm, the maximum absorption intensity of electromagnetic waves reaches −53.5 dB. Furthermore, at a thickness of 3.5 mm, the EAB achieves a maximum of 8.7 GHz. These findings are expected to provide valuable insights into the morphological selection and regulation of magnetic components in dielectric/magnetic composites, contributing to advancements in the development and application of advanced EMA materials. This research has the potential to significantly impact the field of advanced materials by elucidating the intricate processes involved in morphological selection and regulation within these composites.

Electronic Supplementary Material: Supplementary material (SEM images of $CoFe_2O_4$ nanofibers and the aerogel pore structure, digital photo images of the aerogel, XPS spectrum, FTIR spectrum, electromagnetic parameter diagram, attenuation constant diagram, interference loss diagram, aerogel structural destruction interference, and a table of Co and Fe content) is available in the online version of this article at https://doi.org/10.26599/NR.2025.94907142.

Data availability

All data needed to support the conclusions in the paper are presented in the manuscript and the Electronic Supplementary Material. Additional data related to this paper may be requested from the corresponding author upon request.

Acknowledgments

The authors gratefully acknowledge the financial support for this work by the Beijing Municipal Key Fund Project (No. LZY2023043014) and the Fundamental Research Funds for the Central Universities (No.06500100).

Declaration of competing interest

The authors declare no interest conflict. They have no known competing financial interests or personal relationships that could have appeared to influence the work reported in this paper.

Author contribution statement

S. X.: Methodology, validation, formal analysis, investigation, writing – original draft, writing – review & editing. Q. H. L.: Resources, project administration. Z. L. Y.: Investigation. L. J. L.: Investigation. X. D. D.: Conceptualization, resources, writing – review & editing, supervision, funding acquisition. S. Y. Y.: Writing – review & editing, supervision. C. J. L.: Conceptualization, resources, funding acquisition.

Use of AI statement

None.

References

[1] Nia, A. S.; Binder, W. H. Graphene as initiator/catalyst in polymerization chemistry. *Prog. Polym. Sci.* **2017**, *67*, 48–76.

[2] Jimoh, M. F.; Carson, G. S.; Anderson, M. B.; El-Kady, M. F.; Kaner, R. B. Direct fabrication of 3D electrodes based on graphene and conducting polymers for supercapacitor applications. *Adv. Funct. Mater.*, in press, https://doi.org/10.1002/adfm.202405569.

[3] Yang, F.; Deng, P. C.; He, H.; Hong, R. L.; Xiang, K.; Cao, Y.; Yu, B. B.; Xie, Z. M.; Lu, J. M.; Liu, Z. K. et al. Rapid Joule heating-induced welding of silicon and graphene for enhanced lithium-ion battery anodes. *Chem. Eng. J.* **2024**, *494*, 152828.

[4] Almalki, M.; Anagnostou, K.; Rogdakis, K.; Eickemeyer, F. T.; Othman, M.; Stylianakis, M. M.; Tsikritzis, D.; Alanazi, A. Q.; Tzoganakis, N.; Pfeifer, L. et al. Improving the operational stability of perovskite solar cells with cesium-doped graphene oxide interlayer. *J. Energy Chem.* **2024**, *96*, 483–490.

[5] Wu, Y.; Tan, S. J.; Zhang, T. C.; Zhou, M.; Fang, G.; Ji, G. B. Alkali and ion exchange co-modulation strategies to design magnetic-dielectric synergistic nano-absorbers for tailoring microwave absorption. *Nano Res.* **2023**, *16*, 8522–8532.

[6] Han, M. J.; Lan, D.; Zhang, Z. M.; Zhao, Y. Z.; Zou, J. X.; Gao, Z. G.; Wu, G. L.; Jia, Z. R. Micro-sized hexapod-like CuS/Cu_9S_5 hybrid with broadband electromagnetic wave absorption. *J. Mater. Sci. Technol.* **2025**, *214*, 302–312.

[7] Jia, Z. R.; Sun, L. F.; Gao, Z. G.; Lan, D. Modulating magnetic interface layer on porous carbon heterostructures for efficient microwave absorption. *Nano Res.* **2024**, *17*, 10099–10108.

[8] Li, F. S.; Bi, Z. Y.; Kimura, H.; Li, H. Y.; Liu, L. Y.; Xie, X. B.; Zhang, X. Y.; Wang, J.; Sun, X. Q.; Ma, Z. J. et al. Energy- and cost-efficient salt-assisted synthesis of nitrogen-doped porous carbon matrix decorated with nickel nanoparticles for superior electromagnetic wave absorption. *Adv. Compos. Hybrid Mater.* **2023**, *6*, 133.

[9] Shi, Y. X.; Liang, B. Q.; Gao, H.; Zhao, R.; Zhuang, Y. Z.; Guo, Q.; Shao, X. H.; Wang, H. K.; Ma, M. L.; Li, T. X. et al. A lightweight and efficient hollow sunken carbon@MnO_2/reduced graphene oxide composite for high-performance electromagnetic wave absorption. *Chem. Eng. J.* **2024**, *494*, 153252.

[10] Li, F. S.; Wu, N. N.; Kimura, H.; Wang, Y.; Xu, B. B.; Wang, D.; Li, Y. F.; Algadi, H.; Guo, Z. H.; Du, W. et al. Initiating binary metal oxides microcubes electromagnetic wave absorber toward ultrabroad absorption bandwidth through interfacial and defects modulation. *Nano-Micro Lett.* **2023**, *15*, 220.

[11] Xiang, L. L.; Darboe, A. K.; Luo, Z. H.; Qi, X. S.; Shao, J. J.; Ye, X. J.; Liu, C. S.; Sun, K.; Qu, Y. P.; Xu, J. et al. Constructing two-dimensional/two-dimensional reduced graphene oxide/MoX_2 (X = Se and S) van der Waals heterojunctions: A combined composition modulation and interface engineering strategy for microwave absorption. *Adv. Compos. Hybrid Mater.* **2023**, *6*, 215.

[12] Yan, J.; Huang, Y.; Wei, C.; Zhang, N.; Liu, P. B. Covalently bonded polyaniline/graphene composites as high-performance electromagnetic (EM) wave absorption materials. *Compos. Part A: Appl. Sci. Manuf.* **2017**, *99*, 121–128.

[13] Ma, Z. H.; Yang, K.; Li, D.; Liu, H.; Hui, S. C.; Jiang, Y. Y.; Li, S. Y.; Li, Y. M.; Yang, W.; Wu, H. J. et al. The electron migration polarization boosting electromagnetic wave absorption based on Ce atoms modulated yolk@shell Fe_xN@NGC. *Adv. Mater.* **2024**, *36*, 2314233.

[14] Zhang, S. J.; Lan, D.; Zheng, J. J.; Kong, J.; Gu, J. W.; Feng, A. L.; Jia, Z. R.; Wu, G. L. Perspectives of nitrogen-doped carbons for electromagnetic wave absorption. *Carbon* **2024**, *221*, 118925.

[15] Su, J. H.; Zhang, X.; Ma, Z. Q.; Xu, X. Y.; Xu, J.; Chen, Y. J. Construction of Fe_3C@N-doped graphene layers yolk–shelled nanoparticles on the graphene sheets for high-efficient electromagnetic wave absorption. *Carbon* **2024**, *229*, 119448.

[16] Liu, P. B.; Zhang, Y. Q.; Yan, J.; Huang, Y.; Xia, L.; Guang, Z. X. Synthesis of lightweight N-doped graphene foams with open reticular structure for high-efficiency electromagnetic wave absorption. *Chem. Eng. J.* **2019**, *368*, 285–298.

[17] Wang, X. Y.; Lu, Y. K.; Zhu, T.; Chang, S. C.; Wang, W. $CoFe_2O_4$/N-doped reduced graphene oxide aerogels for high-performance microwave absorption. *Chem. Eng. J.* **2020**, *388*, 124317.

[18] Li, W. J.; Li, W. C.; Ma, Z. B.; Kang, Y.; Zou, T.; Lei, Y.; Ying, Y.; Xiang, W. B.; Yu, J.; Zheng, J. W. et al. N atoms regulate heterogeneous crystal phase engineering of mesoporous magnetic Fe_xN nanofibers to promote electromagnetic wave dissipation of magnetic composite aerogel absorbers. *Chem. Eng. J.* **2024**, *481*, 148584.

[19] Chen, W. Q.; Xiao, P. S.; Chen, H. H.; Zhang, H. T.; Zhang, Q. C.; Chen, Y. S. Polymeric graphene bulk materials with a 3D cross-linked monolithic graphene network. *Adv. Mater.* **2019**, *31*, 1802403.

[20] Wu, Y.; An, C.; Guo, Y. R.; Zong, Y. Y.; Jiang, N. S.; Zheng, Q. B.; Yu, Z. Z. Highly aligned graphene aerogels for multifunctional composites. *Nano-Micro Lett.* **2024**, *16*, 118.

[21] Song, X. H.; Chen, Y. Y.; Rong, M. C.; Xie, Z. X.; Zhao, T. T.; Wang, Y. R.; Chen, X.; Wolfbeis, O. S. A phytic acid induced super-amphiphilic multifunctional 3D graphene-based foam. *Angew. Chem., Int. Ed.* **2016**, *55*, 3936–3941.

[22] Zhi, D. D.; Li, T.; Li, J. Z.; Ren, H. S.; Meng, F. B. A review of three-dimensional graphene-based aerogels: Synthesis, structure and application for microwave absorption. *Compos. Part B: Eng.* **2021**, *211*, 108642.

[23] Sun, C. H.; Lan, D.; Jia, Z. R.; Gao, Z. G.; Wu, G. L. Kirkendall effect-induced ternary heterointerfaces engineering for high polarization loss MOF-LDH-MXene absorbers. *Small*, in press, https://doi.org/10.1002/smll.202405874.

[24] Zhu, J. H.; Lan, D.; Liu, X. H.; Zhang, S. H.; Jia, Z. R.; Wu, G. L. Porous structure fibers based on multi-element heterogeneous components for optimized electromagnetic wave absorption and self-anticorrosion performance. *Small*, in press, https://doi.org/10.1002/smll.202403689.

[25] Ma, J. X.; Li, W. H.; Fan, Y. C.; Yang, J. Y.; Yang, Q. K.; Wang, J. C.; Luo, W.; Zhou, W. W.; Nomura, N.; Wang, L. J. et al. Ultrathin and light-weight graphene aerogel with precisely tunable density for highly efficient microwave absorbing. *ACS Appl. Mater. Interfaces* **2019**, *11*, 46386–46396.

[26] Du, W. C.; Wu, M. M.; Zhang, M.; Xu, G. C.; Gao, T. T.; Qian, L.; Yu, X. W.; Chi, F. Y.; Li, C.; Shi, G. Q. High-quality graphene films and nitrogen-doped organogels prepared from the organic dispersions of graphene oxide. *Carbon* **2018**, *129*, 15–20.

[27] Li, Y.; Liu, J. B.; Wang, X. B.; Zhang, X. M.; Chen, N.; Qian, L. T.; Zhang, Y. G.; Wang, X.; Chen, Z. W. $CoFe_2O_4$@rGO as a separator coating for advanced lithium-sulfur batteries. *Small Sci.* **2023**, *3*, 2300045.

[28] Zhang, C. J.; Ma, C.; Zhang, W. W.; Wang, Y. Q.; Rehman, Z. U.; Shen, X. Q.; Yao, S. S. $CoFe_2O_4$ nanoparticles modified amidation of N-doped carbon nanofibers hybrid catalysts to accelerate electrochemical kinetics of Li-S batteries with high sulfur loading. *Chem. Eng. J.* **2024**, *481*, 148374.

[29] Liu, Y. F.; Zhou, G. M.; Sun, Y. X.; Zhang, M.; Ren, T. L.; Wang, L.; Li, C. J. Hollow cobalt ferrite nanofibers integrating with carbon nanotubes as microbial fuel cell anode for boosting extracellular electron transfer. *Appl. Surf. Sci.* **2023**, *609*, 155386.

[30] Xie, X. B.; Wang, B. L.; Wang, Y. K.; Ni, C.; Sun, X. Q.; Du, W. Spinel structured MFe_2O_4 (M = Fe, Co, Ni, Mn, Zn) and their composites for microwave absorption: A review. *Chem. Eng. J.* **2022**, *428*, 131160.

[31] Bourlinos, A. B.; Steriotis, T. A.; Karakassides, M.; Sanakis, Y.; Tzitzios, V.; Trapalis, C.; Kouvelos, E.; Stubos, A. Synthesis, characterization and gas sorption properties of a molecularly-derived graphite oxide-like foam. *Carbon* **2007**, *45*, 852–857.

[32] Kong, X. K.; Wu, P. K.; Tian, S. Y.; Chen, T.; Zhao, S.; Liu, Q. C.; Ju, Z. C. All-in-one: Multi-parameter engineering on γ-Fe_2O_3 for ultra-broadband microwave absorption. *Chem. Eng. J.* **2024**, *485*, 150144.

[33] Cheng, J. Y.; Zhang, H. B.; Wang, H. H.; Huang, Z. H.; Raza, H.; Hou, C. X.; Zheng, G. P.; Zhang, D. Q.; Zheng, Q. B.; Che, R. C. Tailoring self-polarization of bimetallic organic frameworks with

multiple polar units toward high-performance consecutive multi-band electromagnetic wave absorption at gigahertz. *Adv. Funct. Mater.* **2022**, *32*, 2201129.

[34] Lian, Y. Y.; Lan, D.; Jiang, X. D.; Wang, L.; Yan, S.; Dong, Q. Z.; Jiang, Y.; Gu, J. W.; Gao, Z. G.; Wu, G. L. Multifunctional electromagnetic wave absorbing carbon fiber/$Ti_3C_2T_X$ MXene fabric with superior near-infrared laser dependent photothermal antibacterial behaviors. *J. Colloid Interface Sci.* **2024**, *676*, 217–226.

[35] Wang, X.; Chen, X. M.; He, Q. Y.; Hui, Y. Z.; Xu, C. F.; Wang, B. C.; Shan, F. H.; Zhang, J.; Shao, J. Y. Bidirectional, multilayer MXene/polyimide aerogels for ultra-broadband microwave absorption. *Adv. Mater.* **2024**, *36*, 2401733.

[36] Xing, R. Z.; Xu, G. X.; Qu, N.; Zhou, R.; Yang, J. Y.; Kong, J. 3D printing of liquid-metal-in-ceramic metamaterials for high-efficient microwave absorption. *Adv. Funct. Mater.* **2023**, *34*, 2307499.

[37] Zhang, Y.; Lan, D.; Hou, T. Q.; Jia, M. S.; Jia, Z. R.; Gu, J. W.; Wu, G. L. Multifunctional electromagnetic wave absorbing carbon fiber/$Ti_3C_2T_X$ MXene fabric with ultra-wide absorption band. *Carbon* **2024**, *230*, 119594.

[38] Zhang, Y.; Yang, S. H.; Xin, Y.; Cai, B.; Hu, P. F.; Dai, H. Y.; Liang, C. M.; Meng, Y. T.; Su, J. H.; Zhang, X. J. et al. Designing symmetric gradient honeycomb structures with carbon-coated iron-based composites for high-efficiency microwave absorption. *Nano-Micro Lett.* **2024**, *16*, 234.

[39] Yang, N.; Luo, Z. X.; Zhu, G. R.; Chen, S. C.; Wang, X. L.; Wu, G.; Wang, Y. Z. Ultralight three-dimensional hierarchical cobalt nanocrystals/N-doped CNTs/carbon sponge composites with a hollow skeleton toward superior microwave absorption. *ACS Appl. Mater. Interfaces* **2019**, *11*, 35987–35998.

[40] Liu, Y.; Ren, X. Y.; Zhou, X. F.; Lan, D.; Gao, Z. G.; Jia, Z. R.; Wu, G. L. Defect design and vacancy engineering of $NiCo_2Se_4$ spinel composite for excellent electromagnetic wave absorption. *Ceram. Int.* **2024**, *50*, 46643–46652.

[41] Choi, J. R.; Cho, E.; Lee, H.; Lee, S. B.; Yu, W. R.; Kim, J.; Lee, H. J. Synthesis of Fe/Co bimetallic metal-organic framework-derived composites and their enhanced electromagnetic wave absorption. *Adv. Compos. Hybrid Mater.* **2024**, *7*, 26.

[42] Dou, Y. Y.; Zhang, X. Y.; Zhao, X. B.; Li, X.; Jiang, X. H.; Yan, X. F.; Yu, L. M. N, O-doped walnut-like porous carbon composite microspheres loaded with Fe/Co nanoparticles for adjustable electromagnetic wave absorption. *Small* **2024**, *20*, 2308585.

[43] Zhao, T. B.; Lan, D.; Jia, Z. R.; Gao, Z. G.; Wu, G. L. Hierarchical porous molybdenum carbide synergic morphological engineering towards broad multi-band tunable microwave absorption. *Nano Res.* **2024**, *17*, 9845–9856.

[44] Lan, X. L.; Wang, R.; Liu, W. B.; Huang, Z. H.; Deng, P. Y.; Wang, Z. J. Multicomponent synergistic flower-like FeS/hollow C fiber for tunable and efficient microwave absorption. *Chem. Eng. J.* **2024**, *485*, 149238.

[45] Liang, L. Y.; Li, Q. M.; Yan, X.; Feng, Y. Z.; Wang, Y. M.; Zhang, H. B.; Zhou, X. P.; Liu, C. T.; Shen, C. Y.; Xie, X. L. Multifunctional magnetic $Ti_3C_2T_x$ MXene/graphene aerogel with superior electromagnetic wave absorption performance. *ACS Nano* **2021**, *15*, 6622–6632.

[46] Zhou, Z. H.; Zhou, X. F.; Lan, D.; Zhang, Y.; Jia, Z. R.; Wu, G. L.; Yin, P. F. Modulation engineering of electromagnetic wave absorption performance of layered double hydroxides derived hollow metal carbides integrating corrosion protection. *Small* **2024**, *20*, 2305849.

[47] Cheng, Y. H.; Lan, D.; Jia, Z. R.; Gao, Z. G.; Liu, X. H.; Shi, X. T.; He, M. K.; Guo, H.; Wu, G. L. MOF derivatives anchored to multichannel hollow carbon fibers with gradient structures for corrosion resistance and efficient electromagnetic wave absorption. *J. Mater. Sci. Technol.* **2025**, *216*, 150–164.

[48] Xu, J.; Xu, X. Y.; Ma, Z.; Zhang, X.; Yan, F.; Yang, P. P.; Zhu, C. L.; Chen, Y. J. Heterointerface engineering of N-doped graphene aerogels anchored with ultra-small Co and MnO nanoparticles for excellent electromagnetic wave absorption. *Carbon* **2024**, *228*, 119409.

[49] Shao, S. P.; Xing, S. Z.; Bi, K.; Zhao, T. T.; Wang, H.; Tang, Y. X.; Liu, J. R.; Wang, F. L. Fabrication of graphene/polyimide/Co-N-C aerogel with reinforced electromagnetic losses and broadband absorption for highly efficient microwave absorption and thermal insulation. *Chem. Eng. J.* **2024**, *494*, 152976.

[50] Zhao, X. Y.; Sun, X. H.; Wu, W.; Tang, P.; Du, J. W.; Zhang, X. Y.; Qian, H. N.; Peng, R. H.; Wang, X. W.; Zhang, Y. H. et al. rGO aerogel embedded with organic-inorganic hybrid perovskite for lightweight broadband electromagnetic wave absorption. *Nano Res.* **2024**, *17*, 10196–10207.

[51] Shao, S. P.; Guo, C.; Wang, H.; Wang, S. J.; Zhao, T. T.; Tang, Y. X.; Liu, J. R.; Wang, F. L. Multifunctional graphene/$Ti_3C_2T_x$ MXene aerogel inlaid with Ni@TiO_2 core-shell microspheres for high-efficiency electromagnetic wave absorption and thermal insulation. *Chem. Eng. J.* **2024**, *488*, 150918.

[52] Li, B.; Tian, H. Y.; Li, L.; Liu, W.; Liu, J. R.; Zeng, Z. H.; Wu, N. Graphene-assisted assembly of electrically and magnetically conductive ceramic nanofibrous aerogels enable multifunctionality. *Adv. Funct. Mater.* **2024**, *34*, 2314653.

[53] Pu, L.; Li, S. S.; Zhang, Y. W.; Zhu, H. Y.; Fan, W.; Ma, P. M.; Dong, W. F.; Wang, Z. C.; Liu, T. X. Polyimide-based graphene composite foams with hierarchical impedance gradient for efficient electromagnetic absorption. *J. Mater. Chem. C* **2021**, *9*, 2086–2094.

[54] Zhang, X. Y.; Xia, L.; Zhong, B.; Yang, H.; Shi, B.; Huang, L. N.; Yang, Y. N.; Huang, X. X. Three-dimensional reduced graphene oxide/$CoFe_2O_4$ composites loaded with LAS particles for lightweight and enhanced microwave absorption properties. *J. Alloys Compd.* **2019**, *799*, 368–376.